RECyT
Year 27 / Nº 43 / 2025 /
DOI: https://doi.org/10.36995/j.recyt.2025.43.005

Influence of density models on the numerical modeling of natural convection near the water density-inversion point during transient conjugate heat transfer

Influencia del modelo de densidad en el modelado numérico de convección natural cercano al punto de inversión de densidad del agua durante la transferencia de calor conjugado transitoria

Carlos A., Schvezov[1, *]; Alejandro R., Lespinard[2]; Mario R., Rosenberger[1]

1- Instituto de Materiales de Misiones (IMAM), CONICET. Facultad de Ciencias Exactas, Químicas y Naturales. Universidad Nacional de Misiones (UNaM). Felix de Azara 1552 (3300), Posadas, Misiones, Argentina.
2- Instituto Multidisciplinario de Investigación y Transferencia Agroalimentaria y Biotecnología (IMITAB), CONICET. Instituto de Ciencias Básicas y Aplicadas. Universidad Nacional de Villa María. Av. Arturo Jauretche 1555, (5900), Villa María, Córdoba, Argentina.
* E-mail: cschvezov@fceqyn.unam.edu.ar

Received: 02/12/2024; Accepted: 28/04/2025

Abstract
Pasteurization of dairy products using the low temperature, long time (LTLT) method is a simple and cost-effective heat treatment that requires minimal investment, making it suitable for small-scale milk production. However, the cooling stage of pasteurization is often overlooked and rarely considered in process design. This study aims to evaluate heat transfer during the cooling phase of a batch pasteurization process, modeled as two concentric, vertically enclosed cylinders filled with water. For the experiment, the outer enclosure was maintained between 2 ºC and 4 ºC —close to the water density inversion temperature (3.98 ºC)—while the inner enclosure ranged from 63 ºC to 4 ºC. The process was simulated using conjugate heat transfer solvers within the OpenFOAM Finite Volume Method framework. Various water density models were analyzed, compared, and validated against experimental data. Models lacking a density inversion point to accurately simulate this process underestimated the time required for the inner enclosure to reach the final temperature (4 ºC).

Keywords: Conjugate heat transfer; Density-inversion; Finite volume method; Natural convection; Computational fluid dynamics.

Resumen
La pasteurización de productos lácteos mediante el método de baja temperatura y tiempo prolongado es un tratamiento térmico simple y eficaz que requiere de baja inversión, siendo atractivo para la producción de leche a baja escala. Sin embargo, en su diseño del proceso el período de enfriamiento de la pasteurización a menudo no es considerado. El objetivo de este trabajo fue evaluar la transferencia de calor entre dos cilindros cerrados verticales concéntricos llenos de agua durante el proceso de enfriamiento de un tratamiento térmico discontinuo. Para este proceso, la temperatura del recinto exterior osciló entre 2 ºC y 4 ºC, cerca de la temperatura de inversión de la densidad del agua (3,98 ºC), mientras que la temperatura del recinto interno osciló entre 63 y 4 C. Esto se simuló utilizando el método de volumen finito del sofware OpenFOAM mediante algoritmos para transferencia de calor conjugados. Se analizaron, compararon y validaron el uso diferentes modelos de densidad del agua para la simulación con datos experimentales. Los modelos de densidad que no tenían punto de inversión no pudieron modelar este proceso con precisión y subestimaron el tiempo que requiere el recinto interior para alcanzar la temperatura final (4 ºC).

Palabras claves: Transferencia de calor conjugado; Inversión de densidad; Método de volumen finito; Convección natural; Fluidodinámica computacional.

1. Introduction

Long-time low-temperature (LTLT) milk pasteurization is a traditional, simple and effective heat treatment used to reduce mesophilic bacteria populations and eliminate pathogenic microorganisms, thereby enhancing the shelf-life and ensuring consumer safety [1]. The method involves rapidly heating the dairy product to 63 °C, maintaining this temperature for 30 minutes, and subsequently cooling the product quickly. However, in settings involving small-scale regional production, limited technical expertise, or restricted access to modern equipment and utilities, a slight modification of the conventional LTLT method can simplify the process. One of the most practical and hygienic adaptations is to pasteurize pre-packaged dairy products, thus minimizing the risk of post pasteurization contamination during or after packaging [2]. An alternative method is pot pasteurization; however, Dumaslisle, P. et al. (2005) [3] reported that *Escherichia coli* and other bacteria may survive this form of heat treatment. Beyond milk, the LTLT method has also been applied successfully to other food products, including raspberry pulp [4] and crushed tomato [5].

There is limited information available on the cooling stage of LTLT pasteurization for dairy products, as most research has primarily focused on the heating process [5]. According to regional regulations such as the Argentine Food Code [6], the cooling process should be as brief as possible to prevent nutrient degradation, and the final temperature of the dairy product must be at or below 5 ºC (278.15 K). The cooling period is crucial for the product quality, as prolonged cooling can lead to increased nutrient loss and subsequent decline in product quality. Additionally, because microbial inactivation continues during cooling, the thermal profile and its evolution should be considered in the calculation of total pasteurization lethality and F-value. Despite this, the current lethality calculations typically account only for the come-up and holding phases of batch thermal processing. However, in some cases, the cooling phase significantly contributes to the total lethality and should be included in process design considerations to avoid unnecessary overprocessing and degradation of food quality. [5].

The simplest cooling method initially proposed involves immersing the dairy sachet in a water-ice bath under free convection conditions [2]. However, this approach overlooks a key thermodynamic characteristic of water: its density-inversion point near 3.98 ºC. At this temperature, water reaches its maximum density and its volumetric expansion coefficient approaches zero, effectively reversing the direction of the buoyancy force. This inversion significantly hinders heat transfer by free convection when the fluid temperature approaches this point. Specifically, below 3.98 °C, a decrease in temperature leads to a decrease in density, causing the buoyant force to act upward. Conversely, above 3.98 °C, a temperature decrease results in an increase in density, producing a downward buoyant force. At exactly 3.98 °C, the buoyant force is approximately null due to the maximum density of the water. This unique behavior is often neglected in standard buoyancy models used to simulate free convection, despite the fact that buoyancy—driven by local temperature differences— is the primary force driving fluid motion in these scenarios. Therefore, it is essential that density models used in numerical simulations accurately capture the behavior of buoyant forces within the relevant temperature range.

Heat transfer and fluid dynamics in natural convection involving water near its density-inversion point have been extensively studied, particularly in the context of enclosed square cavity. Quintino et al. (2017) [7] reviewed research spanning from 1964 to 2015, highlighting both experimental and numerical studies. These studies commonly involve square cavities oriented at various angles, with opposing hot and cold vertical walls. However, relatively few investigations have examined configurations where the cold surface at the bottom —cases which are particularly relevant for understanding the effects of penetrative convection [8-9]. Most studies adopt simplified water density models, such as the second-degree polynomial proposed by Debbler [10], the potential model by Gebhart & Mollendorf [11], or a fitted fourth-degree polynomial. These models typically span different temperature ranges of 0 – 8 ºC, 0 – 20 ºC and 0 – 40 ºC, respectively.

Other heat transfer studies on natural convection near the anomalous density point of water have investigated a variety of geometrical configurations. These include convection around a horizontal cylinder enclosed in a rectangular cavity [12], within elliptical enclosures [13-14], in eccentric horizontal cylindrical annuli [15], in general annular enclosures [16], in concentric vertical cylinders of different heights [17], and in both concentric and eccentric cylindrical configurations [18-19]. These studies primarily focus on buoyancy-driven flow patterns influenced by the water density-inversion phenomenon, or are applied to processes involving water fusion [20-21].

Additionally, several authors have investigated buoyant heat transfer in enclosed containers containing bluff or internal bodies of various shapes and positions, without strict temperature limitations. A comprehensive review of studies involving enclosed square cavities was presented by Pandey et al. (2019) [22]. Laminar natural convection from heated bodies of different geometries in cubic or spherical enclosures has been examined both numerically and experimentally by Teertstra et al. (2004) [23], Kumar and Mahapatra, 2023 [24] explored natural convection inside a partially open enclosure with a cylindrical obstacle. Heat convection inside a cubic cavity with various heat sources has been studied numerically by Gibanov & Sheremet (2018) [25] and experimentally by Zhan et al. (2019) [26], with a focus on electronic heat dissipation. Furthermore, Priam et al, 2021 [27] provided an example of conjugate natural convection between two fluids.

In standard texts on process engineering and heat transfer, the phenomenon of anomalous density inversion in water is rarely discussed in detail. These references typically apply the Boussinesq approximation [28-30] to model free convection, assuming small density variations and treating them as a linear function of temperature. This is done using a reference temperature and the corresponding volumetric thermal expansion coefficient. However, in the cooling of dairy products where the initial and final product temperatures are 63º C and 5º C, respectively, and the cooling bath temperatures ranges from 0º C and 10º C, this simplification becomes inadequate. Near 3.98º C—where water reaches its maximum density—the volumetric expansion coefficient approaches zero. As a result, the linear approximation fails to accurately capture the non-monotonic behavior of water density, and thus does not adequately represent the heat transfer and fluid dynamics of the system under study.

Based on the considerations above, the aim of this work was to compare buoyancy-driven heat transfer models under free convection during batch LTLT pasteurization using the Finite Volume Method (FVM) and the OpenFOAM v10 multiregion solver. Specifically, the study examined how the choice of density model affects fluid dynamics and heat transfer predictions, particularly in scenarios where the temperature range includes the water density-inversion point. In such cases, inaccurate modeling may lead to erroneous estimations of cooling time or even incorrect conclusions about whether the final target temperature is attainable within design constraints. This, in turn, has implications for the development of accurate industrial control systems. To address this, several density models were evaluated: polynomial functions of temperature (fifth-, third-, second-, and linear-orders) and Boussinesq approximations calculated at different representative temperatures (process average, bath average, and with negative thermal expansion). All other thermophysical properties were modeled as temperature-dependent. The numerical results were validated and compared against experimental data to assess the accuracy of each approach.

2. Materials and Methods

For the analysis conducted in this study, the cooling process was simulated using a single dairy sachet submerged in a water and ice bath contained within a cylindrical enclosure. The sachet was positioned at the axial center of the system. Dynamic simulations were performed using the Finite Volume Method implemented in OpenFOAM v10. The FVM is a numerical technique for solving systems of partial differential equations, enabling the computation of time dependent temperature and velocity vector fields throughout the analyzed volume. This approach contrasts with classical design methods, which typically solve simplified systems of ordinary differential equations (ODEs) and assume spatially homogeneous temperatures. For the purpose of this study, the dairy product was modeled using the thermophysical properties of water. The simulations were evaluated at 30, 60, 120, 360, 600, 900, 1200, 1800, 3000, 3600, and 4000 seconds.

The model was solved using OpenFOAM's multiregion heat transfer solver, *chtMultiRegionFoam*, employing a mixed Euler and Crank-Nicolson time integration scheme with linear interpolation for cell values [31]. The dynamic system was resolved using the PISO (Pressure Implicit with Splitting of Operator) algorithm [32]. Simulations incorporated either fitted density models—expressed as polynomial functions of temperature—or the Boussinesq approximation. The fitted density models were selected and compared based on data from chemical engineering literature.

To determine an appropriate mesh resolution for the FVM simulations, a mesh sensitivity analysis was conducted using a simplified benchmark system: a square cavity with isothermal lateral walls, with the left wall maintained at 283 K and the right wall at 273 K. The resulting velocity and temperature were compared with published data by

Michalek et al. (2005) [33] and Phu & Nguyen (2020) [34] (See appendix A).

2.1. Governing equations

The governing equations used to model natural convection heat transfer between two enclosed fluids were the continuity equation (Eq. 1), the momentum conservation equation (Eq. 2) and the energy conservation equation (Eq. 3). These equations are presented in the form implemented by the OpenFOAM solver. The fluid was assumed to be incompressible, Newtonian, and the flow was considered laminar.

$$\frac{\partial \rho}{\partial t} + \nabla \cdot (\rho u) = 0 \qquad (1)$$

$$\frac{\partial (\rho u)}{\partial t} + \nabla \cdot (\rho u u) = -\nabla p + \nabla \cdot (\mu \nabla u) + \nabla \cdot [\mu (\nabla u)^T] - \frac{2}{3}\mu \nabla (\nabla \cdot u) + \rho g \qquad (2)$$

$$\frac{\partial (\rho h)}{\partial t} + \nabla \cdot (\rho u h) + \frac{\partial (\rho K)}{\partial t} + \nabla \cdot (\rho u K) - \frac{\partial p}{\partial t} = \nabla \cdot (\frac{\kappa}{Cp} \nabla h) + \rho u \cdot g \qquad (3)$$

where ρ is the fluid density; u is the velocity; t is time; p is the pressure; h is the specific enthalpy, calculated as the integral of the specific heat with respect to fluid temperature; K is the kinetic energy, calculated as half the square of the modulus of u; κ is the thermal conductivity and Cp is the specific heat at a constant temperature.

For this analysis, two models for density were proposed. The first represents density as a polynomial function of temperature (detailed in the next section). The second applies the Boussinesq approximation, defined as:

$$\rho = \rho_0 (1 - \beta (T - T_0)) \qquad (4)$$

where β is the thermal expansion coefficient, T_0 is a reference temperature and ρ_0 is the density at the reference temperature.

The temperature dependence of specific heat, dynamic viscosity, and thermal conductivity for water was defined using polynomial equations of third (Eq. 5), fourth (Eq. 6) and second (Eq. 7) degree respectively. The specific heat equation was derived from data in *Fundamentals of Thermal-Fluid Sciences* by Çengel [30]. The viscosity equation was fitted using values derived from *Yaws' Chemical Properties Handbook* [35], within the range 273-500 K. This fitting approach was used to avoid the instabilities that arise when using high-degree polynomials outside their valid temperature range in simulations involving heating processes.

$$Cp = 1112.6 - 60.801T + 0.17589T^2 - 1.9800x10^{-4}T^3 \qquad (5)$$

$$\mu = 0.101358 - 9.72703x10^{-4}T + 3.50981x10^{-6}T^2 - 5.62246x10^{-9}T^3 + 3.36814x10^{-12}T^4 \qquad (6)$$

$$\kappa = -0.2758 + 4.6120x10^{-3}T - 5.5391x10^{-6}T^2 \qquad (7)$$

2.2. Water density models

The values of water density as a function of temperature were taken from Kohlrausch (1986) [36]. In the temperature range from 0 ºC (273.15 K) to 63 ºC (336.15 K), the water density was fitted using a fifth-degree polynomial (P5), which served as the most accurate model to represent density (P5) (Eq. 8). Other models used for comparison were a cubic (P3) (Eq. 9), a quadratic (P2) (Eq.10) and a linear (P1) degree (Eq. 11) polynomial function. These were fitted over the same range as the fifth-degree function, except for the linear model, which was fitted between 0 and 20 ºC, to obtain a more balanced approximation.

$$\rho = -6609.06 + 110.511T - 0.645635T^2 + 0.00190264T^3 - 2.83014x10^{-6}T^4 + 1.69231x10^{-9}T^5 \qquad (8)$$

$$\rho = 86.0224 + 8.19908T - 0.0234154T^2 + 2.06746x10^{-5}T^3 \qquad (9)$$

$$\rho = 708.399 + 2.17349T - 0.00404582T^2 \qquad (10)$$

$$\rho = 1098.57 - 0.347789T \qquad (11)$$

Another model applied to buoyant heat transfer used was the Boussinesq approximation, as described in Eq. 4. For this approximation, three alternatives were evaluated: one at the process average temperature of 31 ºC (304.15 K) (B304), a second one at the bath average temperature of 4 ºC (277.15 K) (B277), close to the point of maximum water density, and a third at 1 ºC (274.15 K) (B274), where volumetric expansion becomes negative. The corresponding values of volumetric expansion used were 3.03 x 10^{-4}, 0.003 x 10^{-4} and -0.5 x 10^{-4} K^{-1}, and the reference densities were 994.03, 999.97 and 999.85 kg m^{-3}, respectively.

2.3. Pasteurizer

The cooling phase of pasteurization was simulated in an insulated cylindrical container

filled with an ice-water bath. The container had a height of 0.15 m and a radius of 0.125 m. A single hot dairy sachet, modeled as a right circular cylinder, was placed at the center of the container, maintaining a 9-mm clearance from the bottom surface to allow fluid circulation underneath. The dairy sachet contained 500 cm^3 of fluid and was modeled as a cylinder with a height of 0.115 m and a radius of 0.0374 m. For the purpose of this study, the fluid within the sachet was assumed to exhibit the thermophysical properties of water.
The dynamic simulation was carried out using the FVM implemented in the OpenFOAM v10 software package [31].

2.3.1. Geometry and mesh

The simulation domain consisted of two concentric cylinders: the outer cylinder, representing the ice-water bath, measured 0.15 m in height and 0.125 m in radius, while the inner cylinder, representing the dairy sachet, measured 0.115 m in height and 0.0374 m in radius. The inner cylinder was positioned concentrically and elevated 9 mm above the bottom surface of the outer container.
The computational domain was divided into two thermally interacting regions: the dairy sachet and the surrounding water bath. These regions exchanged heat, but not mass. The bath region was assumed to be entirely liquid water. Since ice naturally floats on water, the influence of the ice was represented via an upper Robin boundary condition.

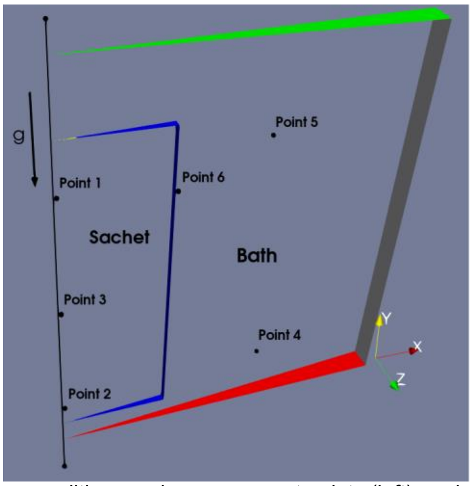

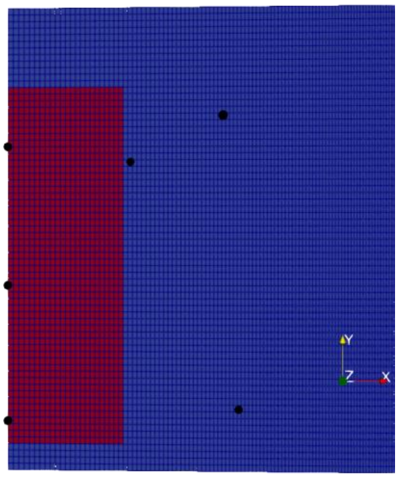

Fig. 1. Boundary conditions and measurement points (left), and structured mesh of the computational domain (right). Bath region (blue) and sachet region (red), and temperature measurement locations (black points).

An axial symmetry was applied; simplifying the problem to a two-dimensional mesh, using the OpenFOAM *wedge* patch. The computational domain was discretized into 6860 structured square cells, of which 5618 belonged to the bath region (Fig. 1b, yellow) and 1242 to the sachet region (Fig. 1b, red). To achieve this configuration, 70 vertical cells and 98 radial cells were defined, with a radial expansion of 0.5, producing a progressively finer mesh near the sachet (see Fig. 1b). This mesh design was informed by the cavity model analysis, using an equivalent average cell size to ensure consistent resolution.
Time steps were variable, adjusted to maintain a Courant Number [31] of up to 0.5 during the first 40 seconds of simulation and up to 1.0 thereafter. A mixed Crank-Nicolson and Euler time integration scheme [31] was applied, with weighting coefficient of 0.9.

2.3.2. Boundary conditions

Ice was modeled as an upper Robin boundary condition, with a fixed normal temperature gradient of 120 K m^{-1}, representing the removal of heat due to the enthalpy of melting, and a fixed temperature value of 273.15 K. In this simulation, ice was not modeled as a separate region, and the resulting meltwater was not considered.
A total pressure of 100 kPa was imposed throughout the domain, with the static pressure calculated as:

$$p = p_0 - 0.5|u|^2 \quad (12)$$

where p_0 is the total pressure and u is the velocity vector. The bottom and external walls of the bath were considered to be adiabatic (insulated). All walls were assigned a no-slip condition, except for the upper Robin boundary, where a slip condition was applied. At the interface between the sachet and the bath, a baffle condition was used with no added thermal resistance, along with a no-slip condition. Heat transfer across the interface was modeled using OpenFOAM's *turbulentTemperatureCoupledBaffleMixed* boundary condition. In this condition, face temperature is evaluated as:

$$T_{\text{face}} = T_1 * \left(\frac{\kappa_1 \Delta_1}{\kappa_1 \Delta_1 + \kappa_2 \Delta_2}\right) + T_2\left(\frac{\kappa_2 \Delta_2}{\kappa_1 \Delta_1 + \kappa_2 \Delta_2}\right) \qquad (13)$$

where the subscripts 1 and 2 refer to the cells of each region, κ is the thermal conductivity, and Δ is the distance from the cell center to the interface. This expression is derived under the assumption of temperature continuity and equal heat flux across the interface.

Due to numerical instabilities caused by heat transfer between two enclosed fluid regions—especially near the beginning of the simulation when the velocity-pressure coupling diverges—four pressure-relief faces were defined at the top center of the sachet interface. These faces had a total radius of 7 mm and were assigned a fixed total pressure of 100 kPa using Equation 12 (see Fig. 1; yellow surface).

The initial conditions were set to 336 K (63 ºC) for the sachet and 275 K (2 ºC) for the bath.

2.3.3. Experimental validation

An experimental setup was developed to obtain temperature profiles for validating the simulation results. Six type-K thermocouples were used: three were inserted along the central vertical axis of the dairy sachet at different heights, and the remaining three were positioned to monitor the temperature of the bath.

A 500-cm³ sachet of raw milk, with a height of 0.115 m, was preheated to 336 K and then submerged within a 6.8-cm³ ice-water bath, with a radius of 0.125 m and an average initial temperature of 2 ºC. Ice was added to maintain thermal conditions, and measurements were recorded until complete melting of the ice. These experimental data were subsequently compared with the simulation results for validation purposes.

3. Results and Discussion

3.1. Comparison of the density models

Figure 2 presents the fitted density models alongside data collected by Kohlrausch [36] and the CRC Handbook [37]. Among the models, only the cubic and fifth-degree polynomials exhibit a maximum density value. According to Kohlrausch's data, the maximum water density is 999.973 kg m^{-3} at 277.05 K, while the CRC Handbook reports a maximum of 999.9749 kg m^{-3} between 277.05 and 277.15 K. In the present study, the maximum values for the cubic and fifth-degree models were 999.952 kg m^{-3} at 275.88 K and 999.969 kg m^{-3} at 277.10 K, respectively. Thus, the fifth-degree polynomial provides a more accurate estimate of the density peak. Furthermore, the average relative error of the fifth-degree model compared with the Kohlrausch and CRC data was 3.6 x 10^{-6} and 1.7 x 10^{-6}, respectively, while the cubic model showed errors of 3.3 x 10^{-5} and 4.1 x 10^{-5}, respectively.

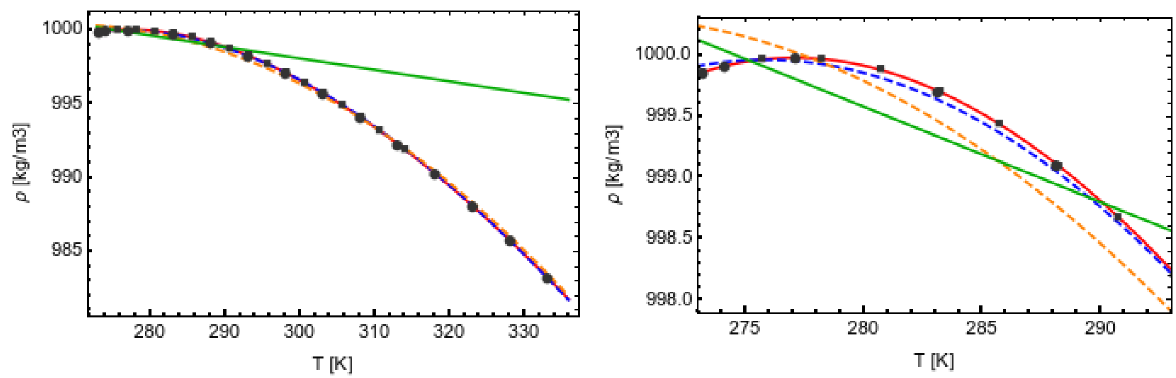

Fig. 2. Comparison between modeled water density as a function of temperature (lines) and collected reference data (points). Models include fifth-degree (red), third-degree (blue), second-degree (orange), and linear (green) polynomial fits, data from Kohlrausch [36] (circles) and CRC Handbook [37] (square).

Several handbooks and educational textbooks were reviewed regarding the treatment of water's anomalous density behavior. Kreith's *Principles of Heat Transfer* [28] provides tabulated data (Table 13) for the properties of liquid water at saturation pressure in 5 K increments. These data include a density inversion point and a negative coefficient of thermal expansion. In contrast, Holman's *Heat Transfer* [29] contains only tabulated values (Table A.9), which do not reflect any density inversion; it also includes Rayleigh number values per cubic meter and per degree Celsius with no negative entries.

Typically, the density of a pure substance is usually modeled using the Rackett equation or a modified version. A model for water density using a modified Rackett equation (Eq. 14) is available in Yaws' *Chemical Properties Handbook* [35]. However, this equation does not feature a mathematical maximum and therefore cannot represent the density inversion of water. Thus, it is unsuitable for modeling free convection heat transfer at low temperatures.

$$\ln(\rho) = \ln(347.1) + (-(1-\frac{T}{647.096})^{0.28571})\ln(0.274) \quad (14)$$

On the other hand, Perry's *Chemical Engineers' Handbook* [38] provides two models for water density: one valid from 273.16 K to 647.096 K, and another from 273.16 K to 353.15 K. These are given in Eqs. 15 and 17, respectively.

$$\rho=(17.863 + 58.606\tau^{0.35} - 95.396\tau^{2/3} + 213.89\tau - 141.56\tau^{4/3})x18.015 \quad (15)$$

$$\tau=(1-\frac{T}{647.096K});T=[273.16;647.096]K \quad (16)$$

$$\rho=(-13.851 + 0.64038T - 0.00191T^2 + 1.8211x10^{-6}T^3) * 18.015;T=[273.16;353.15]K \quad (17)$$

Only the second model (Eq. 17) exhibits a maximum value at 278.83 K with a density of 1003.23 kg m^{-3}, which is 1 K higher and 3 kg m-^{3} greater than the experimental value of 999.973 kg m^{-3} at 277.05 K reported by Kohlrausch. While this discrepancy may be acceptable for modeling natural convection with a cubic approximation, the overestimation is evident in Figure 4 (off by 3 kg m^{-1}). As with other references, Perry's Handbook also includes tabulated values of saturated liquid water properties at 2 K intervals.

3.2. Comparison between simulations with different density models

Figure 3a displays the volume-averaged temperature of the bath as a function of simulation time. At 4000 seconds, the maximum temperature difference between models is approximately 6 K, with the lowest temperature of around 273 K predicted by the B304 model and the highest temperature of around 279 K predicted by the B274 model. Additionally, the temperature profiles of the linear and quadratic models are nearly identical. The linear and B304 models also show similar temperature trends.

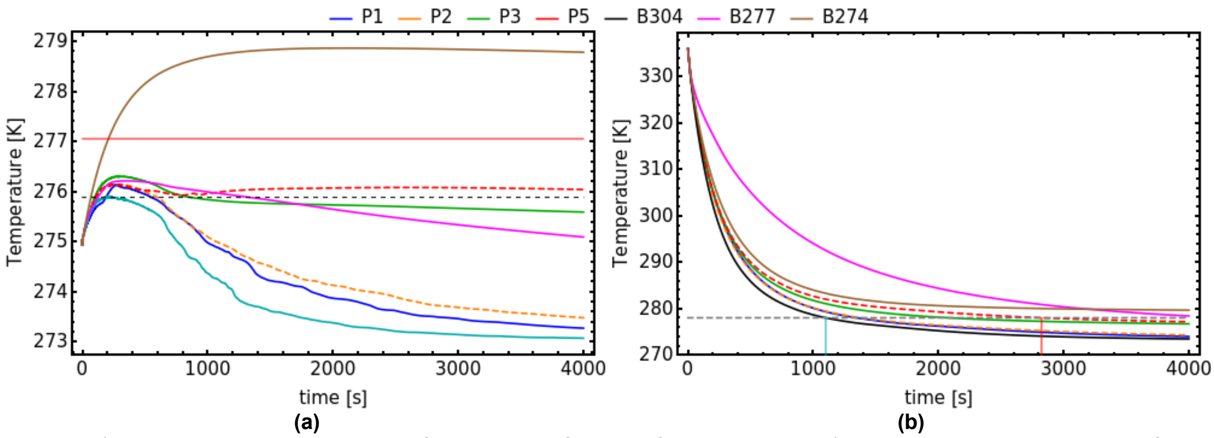

Fig. 3. a) Volume-averaged temperature of the bath as a function of simulation time. b) Volume-averaged temperature of the sachet as a function of simulation time.

Figure 3b shows the volume-averaged temperature profile of the fluid inside the sachet. It can be observed that the B304 model results in the fastest cooling rate, reaching 278 K at 1100 s, whereas the more accurate fifth-degree model reaches the same temperature at 2824 s. In contrast, the B277 and B274 models do not reach the target temperature within the simulated time frame.

Furthermore, the average temperatures of both regions in the linear and quadratic models are nearly similar. The profiles of the average temperature within the bath for the linear and B304 models are also very similar, although the B304 model exhibits a greater cooling rate. The model showing the highest

thermal inertia is B277, as its expansion coefficient is close to zero, which leads to lower convective flow velocities.
For the cubic and fifth-degree models, the bath temperature remains around 275.5 K and 276 K, respectively, for most of the simulation. This behavior is attributed to the density inversion points at 275.88 K and 277.1 K, respectively. Thus, both models—characterized by anomalous density behavior— show similar temperature profiles, with slight differences due to variations in the location of their maximum density points.

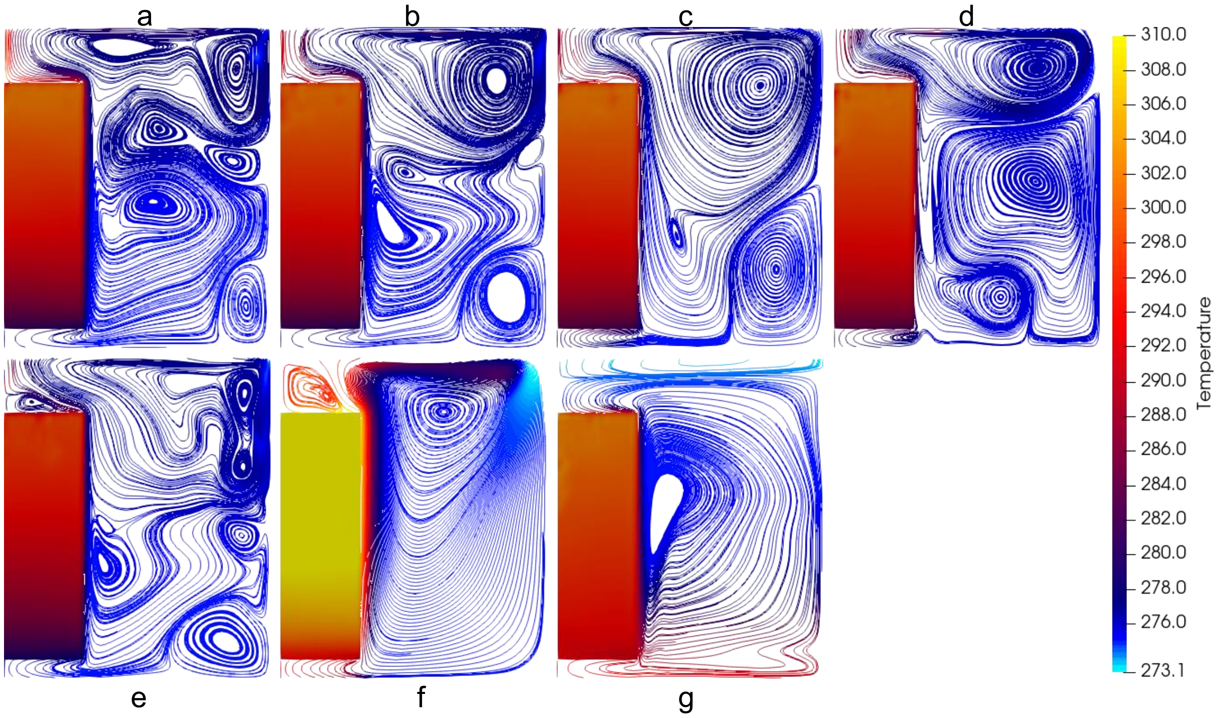

Fig. 4. Streamlines in the bath, colored by temperature, and temperature field within the sachet, at 360 s. a) linear, b) quadratic, c) cubic, d) fifth-degree, e) B304, f) B277 and g) B274.

Figures 4 and 5 display the bath streamlines colored by temperature alongside the temperature gradient within the sachet. These visualizations can be analyzed in conjunction with Figure 6, which shows the bath streamlines colored by the magnitude of the flow velocity. As indicated in Figure 3b, the Boussinesq models B277 and B274 do not reach the target temperature of approximately 278 K, suggesting that the overall heat transfer and flow velocities in these models—visible on Figure 6f and 6g— are lower compared to the other models.
The streamlines shown in Figure 6 help explain the subsequent results. The B277 and B274 models exhibit reduced buoyancy due to the lower absolute values of the volumetric expansion coefficient. In the case of B277, this coefficient is nearly zero, resulting in the slowest overall heat transfer among all models, as illustrated by the velocity scale in Figure 6f. Conversely, the B274 model, which has a negative volumetric expansion coefficient evaluated at 274 K, experiences inverse buoyancy throughout the process. As the temperature rises, the density also increases, causing the warmer fluid to sink and producing a descending temperature gradient. As a result, with the coldest region located at the top of the domain, heat transfer through the upper cold surface occurs primarily via conduction. This leads to lower flow velocities and the stratification of the fluid, as evident in the streamlines and a temperature gradient shown in Figures 5g and 6g.

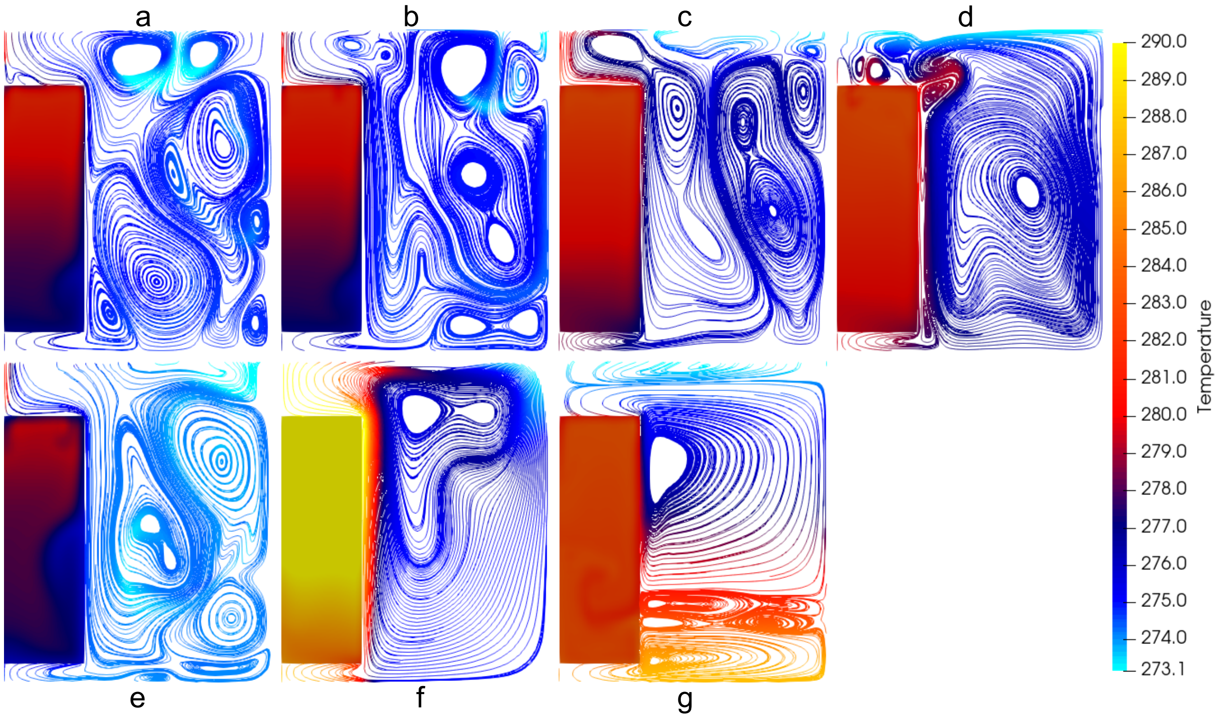

Fig. 5. Streamlines in the bath, colored by temperature, and temperature field within the sachet, at 1200 s. a) linear, b) quadratic, c) cubic, d) fifth-degree, e) B304, f) B277 and g) B274.

Another observation from the streamlines at 1200 s (Figs. 5 and 6,) for the B304 model is that, despite having the lowest average temperature (274.02 K) and a small temperature difference between the cold and hot surfaces, it exhibits the highest fluid velocity. This suggests that, in this case, evaluating fluid properties at the average process temperature is not appropriate for this model—a discrepancy also reflected in the experimental validation. As observed previously, the streamlines indicate reduced diffusion in models with a low thermal expansion coefficient. Nevertheless, the fluid velocity in the B304 model remains the highest among all models analyzed.

The streamlines shown in Figure 5 at 360 s, indicate that the models generally exhibit similar flow patterns, with the exception of those using a low and constant absolute value for the thermal expansion coefficient (B277 and B274). This similarity across models may be attributed to the predominance of local buoyant effects near the sachet wall, which drive the flow regardless of whether the average bath temperature is above or below the density inversion point. Notably, even in the B277 model, where the thermal expansion coefficient is nearly zero and buoyancy acts in the opposite direction, localized buoyant forces still influence the flow near the sachet interface.

Local heat transfer for the seven density models were obtained using OpenFOAM's *wallHeatTransfer postProcess* command. The results, shown in Figure 7, illustrate that at 360 s (Fig. 7a), all models follow a similar overall trend. The B274 model shows notably lower heat transfer along the bottom surface of the sachet. On the lateral wall, heat transfer generally increases with height in all models, with the exception of the B277 model, which maintains a nearly constant value of approximately 3300 W m^{-2}. Conversely, on the upper wall, heat transfer decreases across all models.

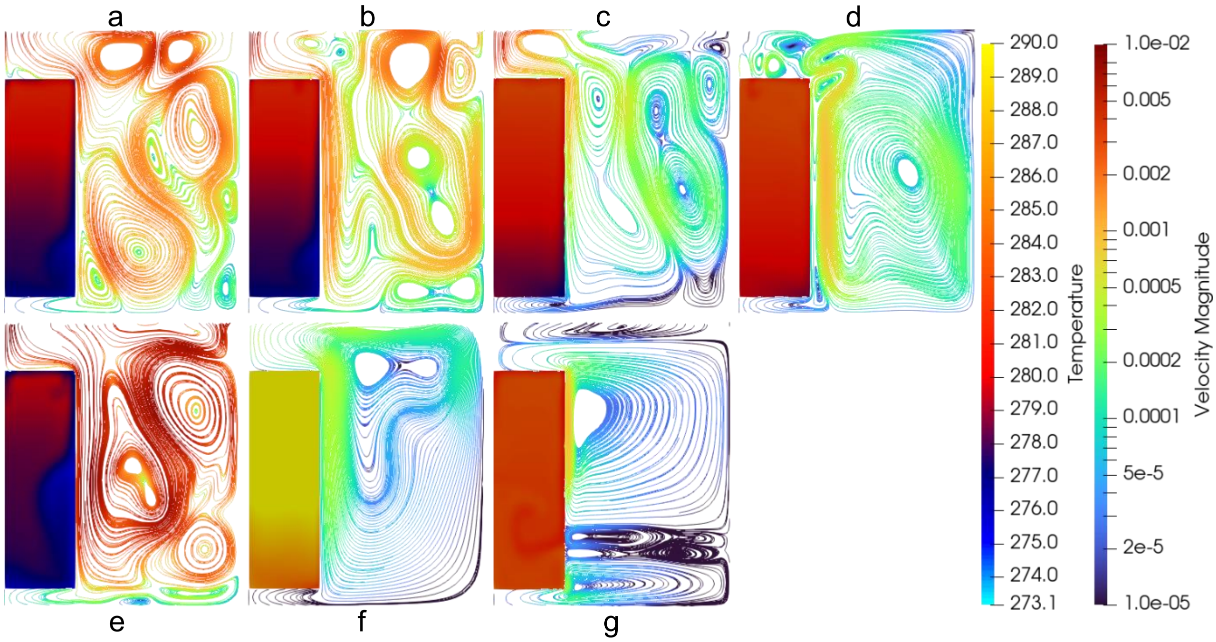

Fig. 6. Streamlines in the bath region colored by the magnitude of flow velocity and temperature field of the sachet, at 1200 s. a) linear, b) quadratic, c) cubic, d) fifth-degree, e) B304, f) B277 and g) B274.

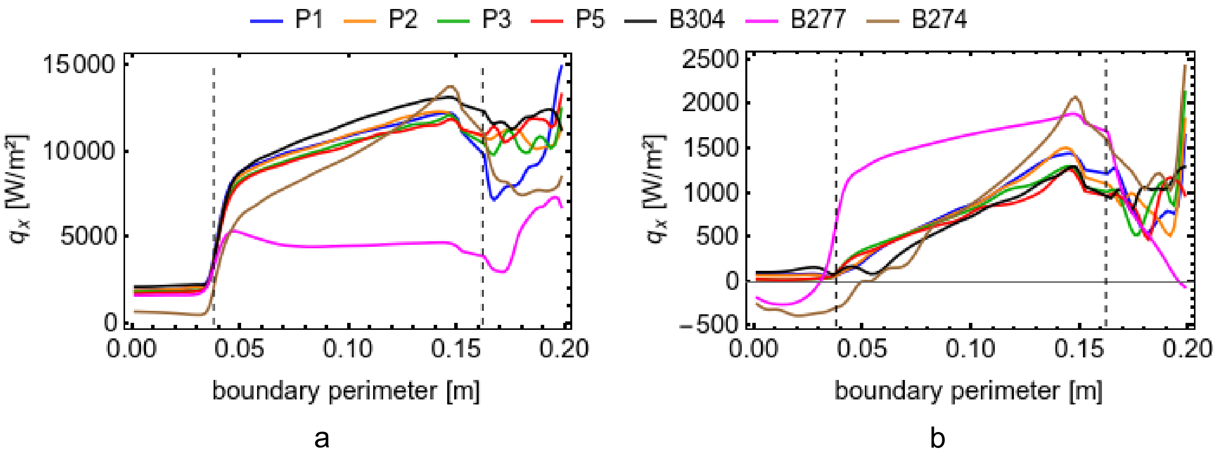

Fig. 7. Local heat transfer along the sachet-bath interface, from bottom to top, at a) 360 s; b) 1200 s and c) 3600 s. Vertical dashed lines indicate the interface vertices, dividing the interface into three regions: bottom, lateral, and top. Positive values represent heat flow from the sachet to the bath; negative values indicate the opposite.

As the simulation progresses to 1200 s (Fig. 7b), reverse heat transfer—from the bath to the product—occurs at the bottom wall of the sachet models with a low thermal expansion coefficient. This effect is primarily is due to thermal stratification within the bath and heat accumulation near its lower region, particularly in the B274 model. Moreover, the sachet is modeled using the fifth-degree density formulation, which causes its lower portion to reach the lowest temperature, thereby generating a reverse temperature gradient. In the case of the b277 model, the reduced circulation velocity leads to similar heat buildup below the sachet, as evidenced by the streamlines (Fig. 6). In contrast, the remaining models show a general decrease in heat transfer, attributed to a diminishing temperature gradient.

3.3. Experimental validation

A comparison between the experimental temperature measurements and the fifth-degree simulation results at three locations inside the sachet (points 1, 2 and 3) is presented in Fig. 8a and detailed in Table 1. Overall, the simulation results show good agreement with the simulation and the experimental data, with average absolute errors of 0.788 K, 1.346 K and 1.324 K for points 1, 2 and 3 respectively. A 95th percentile of the error of 2.127 K, 4.920 K and 2.853 K for the same points, with point 2 showing the largest deviation—primarily during the first 100 seconds. This discrepancy may be attributed to an electrical short circuit in the sensor, movement of the sachet or the thermocouple within the bath, or experimental limitations, such as the opacity of milk, which made visual confirmation inside the sachet impossible. Additionally, Fig. 8a shows a temperature inversion at 2550 s in the simulated data, with point 3 registering the highest temperature and point 1 the lowest.

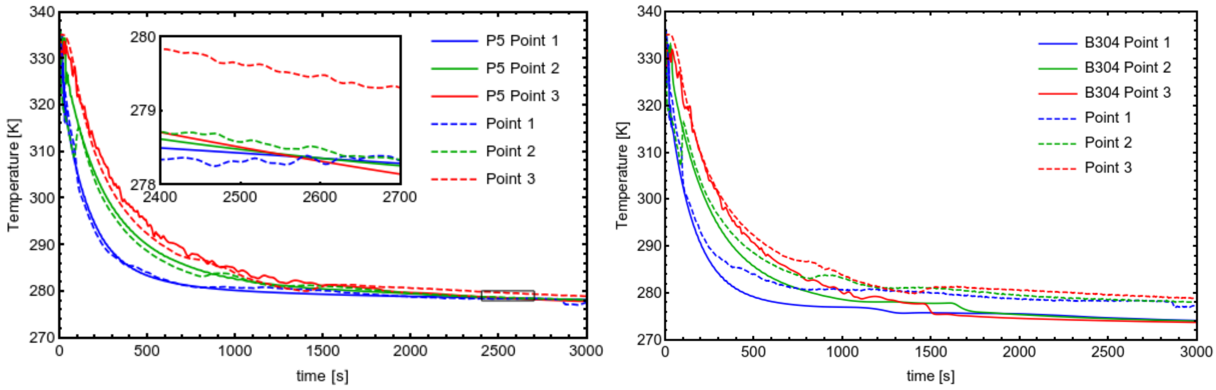

a) b)

Fig. 8. a) Comparison between temperature profiles predicted using a fifth-degree density model and experimental data at three locations (points 1, 2 and 3) within the sachet region. b) Comparison between temperature profiles predicted using a Boussinesq approximation evaluated at 304 K and experimental data at three locations (points 1, 2 and 3) in the sachet region.

As for the other simulations, a comparison between experimental data and the B304 model is shown in Fig. 8b, which demonstrates that this model does not adequately estimate the temperature profile of the process. The simulated temperature begins to deviate from the experimental data after approximately 300 seconds. At 2000 seconds, the simulated temperatures are 3.204 K, 4.120 K and 6.044 K lower than the measured values at points 1,2 and 3, respectively. The average absolute error for these points were 3.911 K, 3.467 K and 2.989 K, respectively, while the 95th percentile errors were 4.931 K, 4.920 K and 6.062 K respectively.

On the other hand, the cubic density model also showed good overall agreement with the experimental data, with average absolute errors of 1.572 K, 1.685 K and 1.288 K for each point. The corresponding 95th percentile errors were 2.204 K, 4.920 K and 2.863 K. The quadratic model yielded higher average absolute errors of 2.660 K, 2.308 K and 1.353 K for each point, with 95th percentile errors of 3.498 K, 4.920 K and 2.897 K, respectively. Additionally, the quadratic model underestimated the final temperature by 3.0 K, 3.7 K and 4.69 K for points 1, 2 and 3, whereas the cubic model underestimated by 0.476 K, 1.291 K and 2.290 K, respectively.

Table 1. Model comparison with experimental data at each measured point. See Figure 1.

	Model	Measured point					
		1	2	3	4	5	6
Average absolute error [K]	P5	0.79	1.35	1.32	1.31	0.65	1.48
	P3	1.57	1.69	1.29	1.76	0.61	0.63
	P2	2.66	2.31	1.35	2.03	1.24	1.67
	B304	3.91	3.47	2.99	2.93	1.76	4.36
95th Percentile of the error [K]	P5	2.13	4.92	2.85	1.81	1.19	1.77
	P3	2.20	4.92	2.86	2.53	1.19	1.42
	P2	3.50	4.92	2.90	3.83	2.67	2.94
	B304	4.93	4.92	6.06	4.66	3.46	6.29
Temperature deviation [K] at 3000 s (experiments minus simulations)	P5	-0.08	-0.57	-1.53	-0.39	-2.30	1.96
	P3	-0.48	-1.29	-2.29	-1.52	-2.12	1.90
	P2	-3.00	-3.70	-4.69	-3.81	-4.44	-0.61
	B304	-4.02	-4.56	-5.45	-4.26	-4.92	-1.25

Similarly, in the bath region, a comparison between the temperatures predicted by the fifth-degree and cubic density models and the experimental temperatures at three points (points 4, 5 and 6) is shown in Figure 9a and 9b, respectively, and detailed in Table 1. The average absolute errors for points 4, 5 and 6 were 1.31 K, 0.653 K and 1.476 K, respectively, while the 95th percentile errors were 1.813 K, 1.186 K and 1.774 K. The discrepancies between the experimental and simulated results may be attributed to simplifications in the geometry—such as modeling the sachet as a perfect cylinder—and the omission of air in the headspace, as well as a possible deviation of the sachet's vertical axis. For points 4 and 5, the simulation slightly underestimated the experimental temperatures; at 3000 s, both models predicted temperatures 1.45 K lower than the experimental values. This discrepancy may result from low insulation in the experimental setup's lateral walls and the fixed gradient used in the model's top boundary condition. In the case of point 6, deviations could stem from minor thermocouple movement, misalignment of the sachet axis, and the assumption of laminar flow in the simulation.

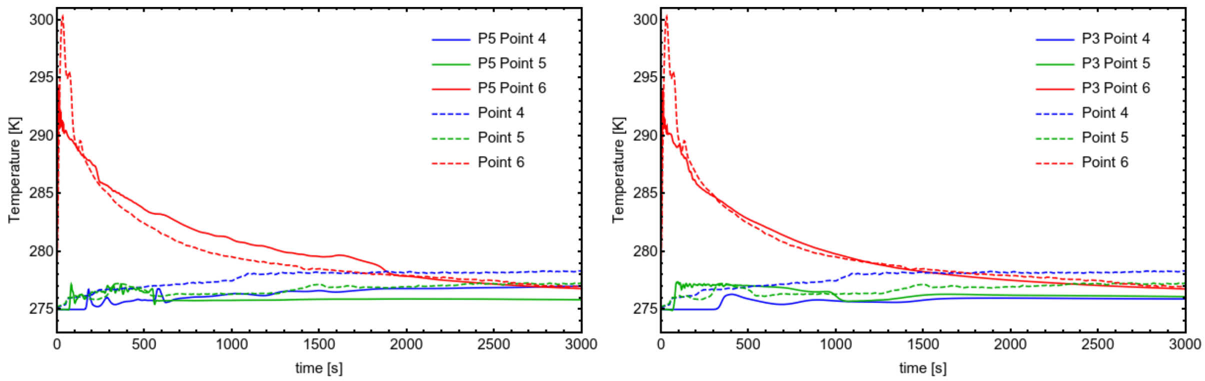

a b

Fig. 9. a) Comparison between temperature profiles predicted with a fifth-degree density model and experimental temperature profiles at three locations (points 4, 5 and 6) in the bath region. b) Comparison between temperature profiles predicted with a cubic density model and experimental temperature profiles at three locations (points 4, 5 and 6) in the bath region.

Nevertheless, the predicted temperature showed overall good agreement with the experimental data, and the temperature trends were consistent. As point 2 is located below point 4, it consistently exhibited a higher temperature, supporting the choice of a density model that includes a density-inversion point for accurately capturing buoyancy-driven heat transfer in the bath. Lastly, point 6 lies within the boundary layer, where a sudden temperature increase is expected; however, the model responds more slowly and fails to capture such rapid transitions.

4. Conclusions

The performance of seven density models—linear, second-degree, third-degree, fifth-degree, B304, B277, and B274—was evaluated over a temperature range of 273 K to 336 K to represent the cooling process near water's density inversion point using a finite volume method. The following conclusions were drawn.

Density models that incorporate a density inversion point—such as the fifth-degree and cubic models presented in this study—proved to be the most accurate in reproducing the experimental results from the pasteurization process. This was consistently validated throughout the simulations. In contrast, the other models failed to accurately predict the final temperatures and the time required to reach them. These findings highlight the critical importance of selecting an appropriate density model that accurately represents fluid behavior across the full temperature range of the simulated process—an aspect often overlooked in some textbooks and handbooks, many of which rely on models lacking a density inversion point. Additionally, this work provided streamlines and temperature profiles for natural convection heat transfer in a cylindrical enclosure with a blunt concentric cylinder filled with fluid.

When the cold plate was positioned at the top, some models—such as linear and quadratic polynomials, as well as the Boussinesq approximation evaluated at 304 K (B304)—

resulted in faster cooling of the pasteurized product. In contrast, other models—including the cubic and fifth-degree polynomials, the Boussinesq approximation at 277 K (B277), and at 274 K (B274)—exhibited delayed cooling due to reduced flow velocity and pronounced stratification effects.
In conclusion, modeling and simulating heat transfer and fluid dynamics in scenarios where the density inversion point lies within the temperature range underscores the importance of selecting appropriate density models—particularly when buoyancy is the primary driving force in the system.

Acknowledgment

This study was completed as part of the *Doctorado en Ciencias Aplicadas*. Universidad Nacional de Misiones, Facultad de Ciencias Exactas, Químicas y Naturales. The author, Carlos Schvezov, acknowledges the Consejo Nacional de Investigaciones Científicas y Técnicas for the scholarship support.

References

1. P. Fellows, *Food Processing Technology: Principles and Practice, Chapter 11: Pasteurisation*. 4th ed., Woodhead Publishing, 2017, p 563.
2. A.M. Martinez, M.R. Rosenberger, Modelado Numérico de Pasteurización Artesanal de Leche y Jugos Naturales, Mecánica Computacional Vol XXXII, (2013) 2485-2501.
3. P. Dumalisile, R.C. Witthuhn, R.J. Britz, Impact of Different Pasteurization Temperatures on the Survival of Microbial Contaminants Isolated from Pasteurized Milk. *Int. J. of Dairy Technol.*, vol. 58, no. 2, May 2005, pp. 74–82. https://doi.org/10.1111/j.1471-0307.2005.00189.x.
4. E.E. Badin, P.E.D. Augusto, R.A. Quevedo-Leon, A. Ibarz, P.D. Ribotta, A.R. Lespinard, *Raspberry Pulp Pasteurization: Computational Fluid Dynamics Modeling and Experimental Validation of Color and Bioactive Compound Retention. J. of Food Process Eng.*, vol. 46, no. 1, Nov. 2022, p. e14168. https://doi.org/10.1111/jfpe.14168.
5. E.E. Badin, M.M. Mercatante, R.H. Mascheroni, R.A. Quevedo-Leon, A. Ibarz, P.D. Ribotta, A.R. Lespinard, Effect of Pasteurization on Color, Ascorbic Acid and Lycopene of Crushed Tomato: A Computational Study with Experimental Validation, *J. of Food Eng.*, vol. 337, Jan. 2023, p. 111218. https://doi.org/10.1016/j.jfoodeng.2022.111218.
6. Código Alimentario Argentino – Capítulo VIII: Alimentos Lácteos. Art. 558.
7. A. Quintino, E. Ricci, S. Grignaffini, M. Corcione, Heat Transfer Correlations for Natural Convection in Inclined Enclosures Filled with Water around Its Density-Inversion Point, *Int. J. of Thermal Sc.*, vol. 116, June 2017, pp. 310–19. https://doi.org/10.1016/j.ijthermalsci.2017.03.008.
8. M. Corcione, A. Quintino, Penetrative convection of water in cavities cooled from below, Comput. and Fluids, vol 123, Dec. 2015, pp 1-9. https://doi.org/10.1016/j.compfluid.2015.09.003.
9. C. Cianfrini, M. Corcione, E. Habib, A. Quintino, Natural Convection of Water Near 4°C in a Bottom-Cooled Enclosure, *Energy Procedia*, vol. 82, Dec. 2015, pp. 322–27. https://doi.org/10.1016/j.egypro.2015.12.040.
10. W.R. Debler, On the Analogy between Thermal and Rotational Hydrodynamic Stability, *Journal of Fluid Mechanics*, vol. 24, no. 1, Jan. 1966, pp. 165–76. *Cambridge University Press*, https://doi.org/10.1017/S0022112066000569.
11. B. Gebhart, J.C. Joseph, A New Density Relation for Pure and Saline Water, *Deep Sea Research*, vol. 24, no. 9, Sept. 1977, pp. 831–48. https://doi.org/10.1016/0146-6291(77)90475-1
12. K. Sasaguchi, K. Kuwabara, K. Kusano, H. Kitagawa, Transient Cooling of Water around a Cylinder in a Rectangular Cavity—a Numerical Analysis of the Effect of the Position of the Cylinder, *Int. J. of Heat and Mass Transfer*, vol. 41, no. 20, Oct. 1998, pp. 3149–56. https://doi.org/10.1016/S0017-9310(98)00064-7.
13. Y.R. Li, Y.P. Hu, X.F. Yuan, Natural Convection of Water Near Its Density Maximum around a Cylinder Inside an Elliptical Enclosure along Slender Orientation, *Numer. Heat Transfer, Part A*, vol. 62, no. 10, Nov. 2012, pp. 780–97. https://doi.org/10.1080/10407782.2012.715978.
14. Y.P. Hu,Y.R. Li, X.F. Yuan, C.M. Wu, Natural Convection of Cold Water near Its Density Maximum in an Elliptical Enclosure

Containing a Coaxial Cylinder, *Int. J. of Heat and Mass Transfer*, vol. 60, May 2013, pp. 170–79. https://doi.org/10.1016/j.ijheatmasstransfer.2012.12.059.
15. C.V. Raghavarao, Y.V.S.S. Sanyasiraju, Natural Convection Heat Transfer of Cold Water in an Eccentric Horizontal Cylindrical Annulus — a Numerical Study, *Comput. Mech.*, vol. 18, no. 6, Dec. 1996, pp. 464–70. Springer Link, https://doi.org/10.1007/BF00350254.
16. Y.P. Hu, Y.R. Li, C.M. Wu, Comparison Investigation on Natural Convection of Cold Water near Its Density Maximum in Annular Enclosures with Complex Configurations, *Int. J. of Heat and Mass Transfer*, vol. 72, May 2014, pp. 572–84. https://doi.org/10.1016/j.ijheatmasstransfer.2014.01.047.
17. M.A. Medebber, R. Noureddine, Numerical Study of Natural Convection in a Vertical Cylindrical Partially Annular, *Mechanics and Mechanical Eng.*, vol. 22, no. 1, Jan. 2018, pp. 77–92. https://doi.org/10.2478/mme-2018-0008.
18. E.M. Sparrow, M. Charmchi. Natural Convection Experiments in an Enclosure between Eccentric or Concentric Vertical Cylinders of Different Height and Diameter, *Int. J. of Heat and Mass Transfer*, vol. 26, no. 1, Jan. 1983, pp. 133–43. https://doi.org/10.1016/S0017-9310(83)80015-5.
19. M. Charmchi, E. M. Sparrow, Analysis of Natural Convection in the Space Between Concentric Vertical Cylinders of Different Height and Diameter, *Numer. Heat Transfer*, vol. 5, no. 2, Apr. 1982, pp. 119–44. https://doi.org/10.1080/10407788208913439.
20. S.L. Braga, R. Viskanta. Effect of Density Extremum on the Solidification of Water on a Vertical Wall of a Rectangular Cavity, *Exp. Therm. and Fluid Sci.*, vol. 5, no. 6, Nov. 1992, pp. 703–13. https://doi.org/10.1016/0894-1777(92)90114-K.
21. C.J. Kim, S.T. Ro, J.S. Lee, M.G. Kim, Two-Dimensional Freezing of Water Filled between Vertical Concentric Tubes Involving Density Anomaly and Volume Expansion, *Int. J. of Heat and Mass Transfer*, vol. 36, no. 10, July 1993, pp. 2647–56. https://doi.org/10.1016/S0017-9310(05)80201-7.
22. S. Pandey, Y.G. Park, M.Y. Ha, An Exhaustive Review of Studies on Natural Convection in Enclosures with and without Internal Bodies of Various Shapes, *Int. J. of Heat and Mass Transfer*, vol. 138, Aug. 2019, pp. 762–95. https://doi.org/10.1016/j.ijheatmasstransfer.2019.04.097.
23. P.M. Teertstra, M.M. Yovanovich, J.R. Culham, Models and Experiments for Laminar Natural Convection From Heated Bodies in Enclosures, Volume 1, ASMEDC, 2004, pp. 443–53. https://doi.org/10.1115/HT-FED2004-56633.
24. S. Kumar and S.K. Mahapatra. An Experimental and Numerical Analysis of Natural Convection in a Partially Open Cuboid Enclosure with a Cylindrical Obstacle. *Therm. Sci. and Eng. Prog.*, vol. 45, Oct. 2023, p. 102118. https://doi.org/10.1016/j.tsep.2023.102118.
25. N.S. Gibanov, and M.A. Sheremet. Natural Convection in a Cubical Cavity with Different Heat Source Configurations. *Therm. Sci. and Eng. Prog.*, vol. 7, Sept. 2018, pp. 138–45. https://doi.org/10.1016/j.tsep.2018.06.004.
26. N. Zhan, L. Ding, Y. Chai, J. Wu and Y. Xu. Experimental Study on Natural Convective Heat Transfer in a Closed Cavity. *Therm. Sci. and Eng. Prog.*, vol. 9, Mar. 2019, pp. 132–41. https://doi.org/10.1016/j.tsep.2018.11.009.
27. S.S. Priam, M.Md. Ikram, S. Saha and S.C. Saha. Conjugate Natural Convection in a Vertically Divided Square Enclosure by a Corrugated Solid Partition into Air and Water Regions. *Therm. Sci. and Eng. Prog.*, vol. 25, Oct. 2021, p. 101036. https://doi.org/10.1016/j.tsep.2021.101036.
28. F. Kreith, R.M. Manglik, M.S. Bohn, *Principles of Heat Transfer 7th Edition*, Appendix 2: Data Tables, Table 13. Cengage Learning, 2011, p. A14.
29. J.P. Holman, *Transferencia de Calor*. 1st ed., Apéndice A, Tabla A9, McGraw-Hill, 1986, pp 600.
30. Y.A. Cengel, J.M. Cimbala, R.H. Turner, *Fundamentals of Thermal-Fluid Sciences 5th de., Appendix 1: Property Tables and Charts (SI units), Table A-15*, McGraw-Hill, New York, 2017, p. 994.
31. C. Greenshields, H. Weller. Notes on computational fluid dynamics: General principles, CFD Direct Ltd, Reading, UK, 2022.
32. R.I. Issa, Solution of the Implicitly Discretised Fluid Flow Equations by Operator-Splitting, *J. of Comput. Phys.*, vol.

62, no. 1, Jan. 1986, pp. 40–65. https://doi.org/10.1016/0021-9991(86)90099-9.

33. T. Michalek, T.A. Kowalewski, B. Sarler, Natural Convection for Anomalous Density Variation of Water: Numerical Benchmark, *Progress in Computational Fluid Dynamics, An International Journal*, vol. 5, no. 3/4/5, 2005, p. 158-169. https://doi.org/10.1504/PCFD.2005.006751.

34. M.P. Nguyen, N. Van Hap, Computational Overview of Fluid Structure Interaction, *Numerical Investigation of Natural Convection and Entropy Generation of Water near Density Inversion in a Cavity Having Circular and Elliptical Body*. IntechOpen, 2020. *www.intechopen.com*, https://doi.org/10.5772/intechopen.95301.

35. C.L. Yaws, *Chemical Properties Handbook: Physical, Thermodynamic, Environmental, Transport, Safety, and Health Related Properties for Organic and Inorganic Chemicals*. McGraw-Hill, 1999.

36. F. Kohlrausch, *Praktische Physik*, Band 3 – Tabellen und Diagramme, 23 Auflage, Table 65, B.G. Teubner Stuttgart, 1986, pp 88 – 90.

37. W.M. Haynes, Ed., *CRC Handbook of Chemistry and Physics 97th ed*., Section 6: Fluid Properties, CRC Press, Boca Raton, FL, 2017, pp 6-1 – 6-2.

38. D.W. Green, Ed., *Perry's Handbook of Chemical Engineer 8th Edition,* Section 2 Physical and Chemical Data, Table 2-32, McGraw-Hill, 2008; pp 2-103.

Appendix. Free convection inside a cavity

A square enclosed cavity model was developed to validate the appropriate water density model and mesh resolution. The cavity measured 38 mm by 38 mm, with the left wall maintained at a constant temperature of 10 ºC (283.15 K) and the right wall at 0 ºC (273.15 K). The upper and lower walls were thermally insulated and a no-slip boundary condition was applied to all walls. The cavity was discretized using a regular square mesh of 160 by 160 cells, totaling 25,600 cells. A coarser mesh of 16 by 16 cells was also simulated to assess the influence of mesh size on the results. For the simulations, the governing equations (Eqs. 1– 3, 5) and thermophysical property relations (Eqs. 5-8) were employed.

The results were compared with those reported by Michalek et al. (2005) [33] and Phu & Nguyen (2020) [34]. To facilitate this comparison, dimensionless numbers along both the vertical and horizontal centerlines of the cavity were analyzed. The dimensionless quantities used in the analysis were:

(Eq. A.1 – A.4)

where x and y are the horizontal and vertical coordinates, respectively; L is the length of the cavity, Ux and Uy are the horizontal and vertical components of the velocity vector, respectively; and α is the thermal diffusivity.

Figure A.1 presents the comparison through dimensionless velocity components along the central horizontal plane: Figure A.1a shows the horizontal component of the dimensionless velocity as a function of cavity length, while Figure A.1b displays the vertical component. As observed, the simulation results obtained using the refined mesh exhibit good agreement with those reported by Michalek et al., particularly near the center of the cavity. In contrast, the results from the coarser mesh display noticeable discrepancies, especially in the central region.

Figure A.2 displays the streamlines resulting from simulations performed with both coarse and refined meshes. The figure clearly illustrates that the coarse mesh fails to accurately capture the formation and structure of the vortices, in contrast to the refined mesh, which provides a more precise representation of the flow field. These findings support the conclusion that the average cell size used in the refined mesh is appropriate and can be reliably applied in the other simulations conducted in this study.

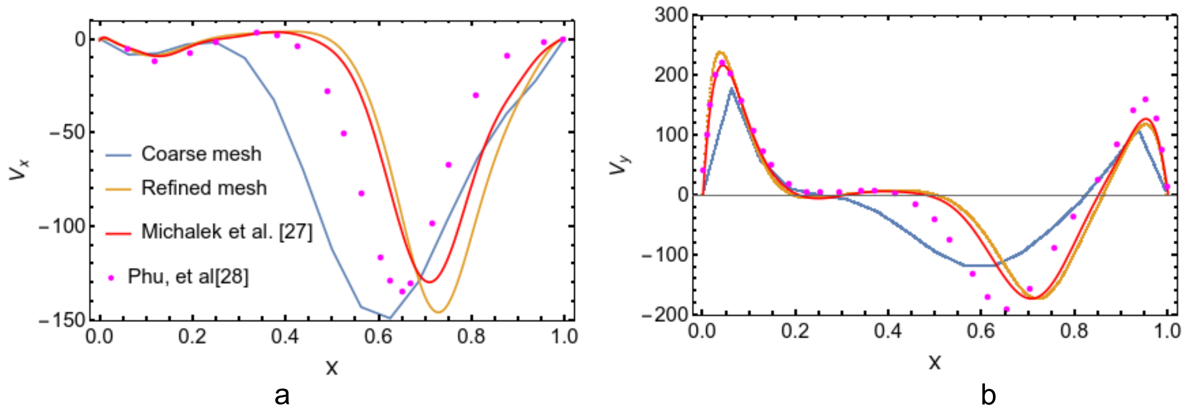

Fig. A.1. Dimensionless velocity along the central horizontal plane. x component (a), y component (b). Blue: coarse mesh simulation, orange: refined mesh, magenta dots: Nguyen data [34], red: Michalek data [33].

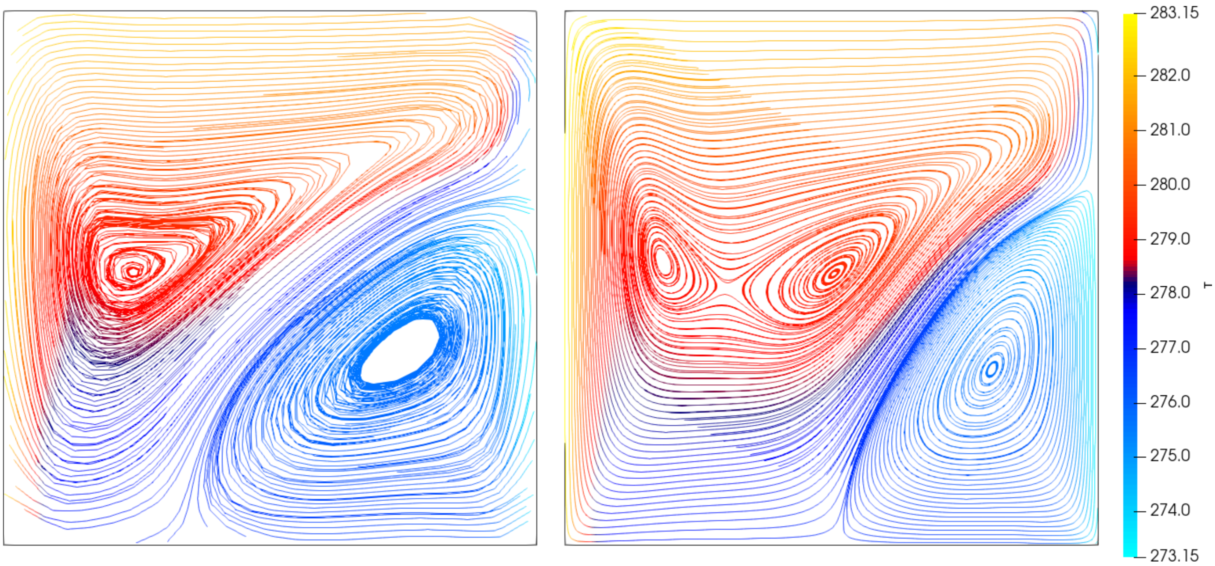

Fig. A.2. Streamlines colored by temperature. Left: coarse mesh simulation; right: refined mesh simulation.